Transfer of a Rational Crystal Contact Engineering Strategy between Diverse Alcohol Dehydrogenases

Brigitte Walla [1], **Daniel Bischoff [1]**, **Robert Janowski [2]**, **Nikolas von den Eichen [1]**, **Dierk Niessing [2,3]** **and Dirk Weuster-Botz [1,*]**

[1] Institute of Biochemical Engineering, Technical University of Munich, Boltzmannstraße 15, 85748 Garching, Germany; brigitte.walla@tum.de (B.W.); daniel.bischoff@tum.de (D.B.); nikolas.eichen@tum.de (N.v.d.E.)

[2] Institute of Structural Biology, Helmholtz Zentrum München, Ingolstädter Landstraße 1, 85764 Neuherberg, Germany; robert.janowski@helmholtz-muenchen.de (R.J.); niessing@helmholtz-muenchen.de (D.N.)

[3] Institute of Pharmaceutical Biotechnology, Ulm University, James Franck Ring N27, 89081 Ulm, Germany

[*] Correspondence: dirk.weuster-botz@tum.de

Abstract: Protein crystallization can serve as a purification step in biotechnological processes but is often limited by the non-crystallizability of proteins. Enabling or improving crystallization is mostly achieved by high-throughput screening of crystallization conditions and, more recently, by rational crystal contact engineering. Two selected rational crystal contact mutations, Q126K and T102E, were transferred from the alcohol dehydrogenases of *Lactobacillus brevis* (*Lb*ADH) to *Lactobacillus kefir* (*Lk*ADH). Proteins were expressed in *E. coli* and batch protein crystallization was performed in stirred crystallizers. Highly similar crystal packing of *Lk*ADH wild type compared to *Lb*ADH, which is necessary for the transfer of crystal contact engineering strategies, was achieved by aligning purification tag and crystallization conditions, as shown by X-ray diffraction. After comparing the crystal sizes after crystallization of *Lk*ADH mutants with the wild type, the mean protein crystal size of *Lk*ADH mutants was reduced by 40–70% in length with a concomitant increase in the total amount of crystals (higher number of nucleation events). Applying this measure to the *Lk*ADH variants studied results in an order of crystallizability T102E > Q126K > *Lk*ADH wild type, which corresponds to the results with *Lb*ADH mutants and shows, for the first time, the successful transfer of crystal contact engineering strategies.

Keywords: technical protein crystallization from impure sources; rational crystal contact engineering; downstream processing; crystal image analysis

1. Introduction

Nowadays, protein crystallization is mainly used for crystallography to obtain the structural information of biological macromolecules. However, growing well-diffracting protein crystals for X-ray analysis is still challenging. There are numerous commercially available high-throughput screening kits that can be used to vary extrinsic conditions like pH, buffer type, ionic strength, or precipitant type for receiving protein crystals [1]. However, the optimization of protein crystallization remains a mainly empirical process [2] and improved crystallization conditions apply almost exclusively to a specific protein or protein family. Thus, the protein itself might be the most important variable for a more general optimization of crystallization [3].

Changing intrinsic characteristics by protein engineering to obtain protein crystals (for X-ray crystallography) has been conducted since the early 1990s [4–7]. Exchanging amino acids at the solvent-exposed surface of proteins has been investigated in several studies [3,8–12]. Derewenda et al. developed the surface entropy reduction (SER) strategy, in which exposed amino acids with high conformational entropy (Lys, Glu, Gln) are exchanged to an amino

acid with low conformational entropy (Ala), in order to enhance crystallizability [3,9,13]. This approach was expanded by suggesting further amino acids for the exchange, including tyrosine and threonine [10]. An alternative approach to improve crystallization by engineering the solvent-exposed protein surface is to introduce metal binding sites between symmetry-related macromolecules by inserting aspartic acid or histidine-cysteine pairs for coordinating heteroatoms (Ca^{2+}, Zn^{2+}) [14–16]. Furthermore, introduced cysteines at the protein surface can form disulfide bonds for dimer stabilization as a precursor for nucleation [17]. However, these studies were primarily aimed at producing large, singular crystals sufficient for structural analysis by X-ray crystallography.

A further interesting field of application for protein crystallization is its use as a purification and/or capture step in industrial downstream processing [18]. Protein purification by diffusion controlled preparative chromatography is a cost-intensive bottleneck in downstream processing. Consequently, the replacement of this purification step with a comparatively less cost-intensive crystallization step offers great economical potential (reviewed in [18,19]). In addition, protein crystallization allows a dense and highly concentrated, as well as pure formulation with a longer shelf life and sustained enzymatic activity [20–22]. Probably the most well-known technical application of protein crystallization is the production of crystalline recombinant insulin [21,23]. However, despite advantages for technical applications, protein crystallization has so far barely been integrated in biotechnological downstream processes [24].

Previous studies focused on enforcing intermolecular interactions during crystallization specifically at crystal contact areas to increase protein crystallization for technical purposes. Studies were performed with the technically relevant enzyme *Lactobacillus brevis* alcohol dehydrogenase (*Lb*ADH) [24–27]. In addition to the general SER strategy of Derewenda et al., aromatic interactions as well as electrostatic interactions at specific preselected crystal contacts were investigated. This rational protein engineering at crystal contact areas resulted in *Lb*ADH mutants with enhanced crystallizability, compared to *Lb*ADH wild type, without changing enzymatic activity. In the same study, "enhanced crystallizability" was defined by an increased number of protein crystals in batch processes at fixed process times, concomitant to increased nucleation rate, reduced induction time of crystallization, and a reduced time span until crystallization equilibrium [24]. In order to be able to trace changes in crystallizability back to this distinct amino acid exchange and avoid unintended changes of crystal contact areas compositions, the formation of highly similar crystal contact areas is a prerequisite [25].

The aim of this study is to transfer protein engineering strategies at crystal contact areas, which were developed for *Lb*ADH, to a different protein, the *Lactobacillus kefir* alcohol dehydrogenase (*Lk*ADH) with an amino acid sequence homology of 88.5% (Supplementary Figure S1). The purpose is to demonstrate that rational protein engineering at crystal contacts leading to enhanced crystallizability can be transferred to homologous proteins. However, similar to crystal contact engineering, the prerequisite of a rational transfer is high similarity in crystal packing. The initial focus of this study will be on the alignment of the crystal packing of *Lk*ADH to *Lb*ADH. Based on the same crystal structure, the transfer of enhanced crystallizability will be demonstrated with the example of introduced electrostatic interactions at a selected crystal contact area. With regard to the application as a purification/capture step in downstream processing, stirred protein crystallization from clarified *E. coli* cell lysate will be investigated for the *Lk*ADH wild type, as well as *Lk*ADH mutants.

2. Materials and Methods

2.1. Mutagenesis

The enzyme *Lactobacillus kefir* alcohol dehydrogenase (*Lk*ADH) was selected for the transfer of a successful crystal contact engineering strategy established with *Lactobacillus brevis* alcohol dehydrogenase (*Lb*ADH). The His-tag and linker sequence of a *Lk*ADH variant (PDB ID: 4RF4, [28]) was replaced with a N-terminal His$_6$ sequence, followed by a

glycine-serine-glycine (GSG) linker sequence identical to the *Lb*ADH wild type studied before (PDB ID: 6H07, [27]). The *E. coli* codon optimized gene was synthesized by Integrated DNA Technologies Inc. (IDT, Leuven, Belgium) using Gibson assembly. The synthesized gene fragment was cloned into DNA expression plasmid pET28a(+) via restriction digest with endonucleases *NcoI* and *HindIII*, resulting in His$_6$_GSG_*Lk*ADH construct (*Lk*ADH wild type). Site-directed mutagenesis was conducted for *Lk*ADH mutants T102E and Q126K according to the standard QuikChange PCR protocol. Primers were designed according to adaptions of Zheng et al. [29]. Partial overlapping primers used for *Lk*ADH mutant T102E were 5′-GATACC**GAG**ACAGAAGAATGGC-3′ and 5′-CAACTTCTATGG**CTC**TGTCTTC-3′, for Q126K 5′-GGTATT**AAG**CGTATGAAAAA-CAAAGG-3′ and 5′-CAGACCCATAA**TTC**G-CATAC-3′ (mutagenized positions are denoted in boldface). After PCR product preparation (FastGene® Gel/PCR Extraction Kit, Nippon Genetics Europe GmbH, Düren, Germany) and *DpnI* digest, the amplified plasmid was transformed into DH5α chemo-competent cells and inoculated on Luria-Bertani (LB) plate containing 35 µL mL^{-1} kanamycin. *E. coli* colonies, which incorporated the mutated plasmid, were selected by colony PCR (FastGene Optima HotStart Ready Mix, Nippon Genetics Europe GmbH, Düren, Germany). Plasmids of *Lk*ADH mutants were isolated via mini-prep and sequenced by IDT with standard primer petup and T7term.

2.2. Protein production and Purification

For heterogeneous protein production in *E. coli*, *Lk*ADH plasmid was transformed into expression strain BL21(DE3). Analogous to Nowotny et al. [25], 5 mL of preculture was grown for 18 h in terrific broth (TB) medium, containing 35 µL mL^{-1} kanamycin (180 rpm, 30 °C). Then, 0.5 L shake flasks filled with 100 mL TB medium (35 µL mL^{-1} kanamycin) were inoculated with preculture (final OD$_{600}$ of 0.05) and incubated at 30 °C and 230 rpm until an OD$_{600}$ of 0.6–0.8 was reached. *Lk*adh gene expression was induced by addition of 200 µM isopropyl ß-D-1-thiogalactopyranoside. After 20 h of *Lk*ADH protein production (20 °C, 230 rpm), the cells were harvested by centrifugation (1500× *g*, 4 °C, 10 min) and stored at −20 °C for further use. For µL-scale batch crystallization and enzymatic activity measurements (as described below), the harvested cells were disrupted via sonication, the cell lysate was centrifuged for clarification, the *Lk*ADH protein was purified by immobilized metal ion affinity chromatography (IMAC) and dialyzed against protein buffer (20 mM HEPES/NaOH pH 7.0, 1 mM MgCl$_2$).

2.3. Protein Crystallization

To obtain the *Lk*ADH wild type protein crystal structure, protein crystallization in µL-scale was conducted with purified protein according to Nowotny et al. [25] (0.1 M Tris/HCl pH 7.0, 75 mM MgCl$_2$, polyethylene glycol (PEG) MME 550 or 3000). A theoretical molar extinction coefficient of 23,950 M^{-1} cm^{-1} (calculated with ProtParam; [30]) was used for protein concentration determination.

For parallel crystallization experiments with non-purified *Lk*ADH variants, harvested cells were processed according to Grob et al. [24]. Crystallization experiments with clarified (phosphate-buffered saline, pH 7.4) and subsequently dialyzed (20 mM HEPES/NaOH pH 7.0, 1 mM MgCl$_2$) cell lysate were conducted in up to eight parallel 5 mL stirred tank reactors with a stirrer speed of 150 rpm, as described in Smejkal et al. [31]. The parallel stirred tank crystallization reactors were adapted from Hebel et al. [32]. Pitched-blade impellers were printed using an MSLA 3D printer (Prusa SL1, Prusa Research a.s., Prague, Czech Republic) from biocompatible epoxy resin (Bio ENG3, 3Dreysns, Barcelona, Spain) with a layer height of 50 µm and an initial exposure time of 35 s (exposure time for all subsequent layers was 12 s). The stirrers were printed directly onto the build plate, with lateral supports for better build plate adhesion. After printing, the stirrers were cleaned and UV cured. Control of the stirrers was implemented with a custom-built control unit based on two six-axis stepper motor driver modules (TMCM6110, Trinamic, Hamburg,

Germany) that controlled up to 12 stepper motors simultaneously. Microstepping enabled smooth stirrer rotation between 1 and 2000 rpm.

Before initiation of crystallization, the absorption of the samples was measured spectrophotometrically at 280 nm and adjusted to similar values with protein buffer. The samples were filtered through a 0.2 μm polypropylene syringe filter to remove particles, which might function as heterogeneous crystallization nuclei. To adjust its temperature, 2.5 mL of filtered protein solution was transferred to a 5 mL crystallizer in a temperature-controlled water bath at 20 °C. Protein crystallization was initiated by the addition of 2.5 mL crystallization buffer (0.1 M Tris/HCl pH 7.0, 50 mM $MgCl_2$, 200 g L^{-1} PEG MME 550) to the prepared protein solution, resulting in a protein concentration defined as initial protein concentration c_0, and monitored for 48 h with regular intervals of sampling.

2.4. Protein Analytics and Analysis of Crystal Photomicrographs

The protein purity of collected IMAC fractions was validated by discontinuous sodium dodecyl sulphate polyacrylamide gel electrophoresis (SDS-PAGE). Enzymatic activity of purified *Lk*ADH variants was determined spectrophotometrically as described in Grob et al. [24]. The oxidation of acetophenone to R-1-phenyl alcohol catalyzed by *Lk*ADH was detected at 340 nm by stoichiometric reduction of NADPH/H$^+$ to NADP$^+$.

Stirred *Lk*ADH protein crystallization in 5 mL reactors was analyzed with bicinchoninic acid (BCA) protein assay for total protein concentration of the supernatant. A discontinuous SDS-PAGE was used for validation of similar *Lk*ADH protein concentrations between samples and densitometrical measurement of crystallization yield. To prevent further crystal growth or nucleation, protein solutions were diluted 10-fold with protein buffer directly after sampling. For the analysis of crystal photomicrographs, samples were taken after 48 h of protein crystallization and diluted 10-fold. A 10 μL drop placed in a crystallization plate (MRC UnderOil Crystallization Plate, SWISSCI, Neuheim, Switzerland) was monitored microscopically inside an incubator (KB115, Binder, Tuttlingen, Germany) at 20 °C. Photomicrographs were taken automatically by a digital camera (DS-Fi3) attached to a light microscope (Nikon Eclipse 50i with 4-fold objective (CFI Plan Fluor), Nikon, Düsseldorf, Germany), controlled by NIS Elements AR v.5.02 imaging software (Nikon, Düsseldorf, Germany).

2.5. X-ray Diffraction and Data Refinement

Diffraction data were collected at the Swiss Light Source (SLS) synchrotron beamline X06DA (PXIII), using a PILATUS 2M-F detector. All crystals were soaked in 25–30% (*v/v*) ethylene glycol for cryo-protection and then mounted on a nylon fiber loop and flash-frozen in liquid nitrogen. X-ray data collection was performed at 100 K [33]. Diffraction spots were integrated and indexed with *XDS* [34]. Refinement was performed with the CCP4 suite [35]. The structure of the previously published *Lk*ADH wild type (PDB ID: 4RF4) was used as the search model for molecular replacement with PHASER [36] and the model was then refined using COOT [37] and REFMAC [38]. The final model and structure factors have been deposited in the Protein Data Bank (PDB) under identification code (ID) 7P36 for the *Lk*ADH wild type with transferred crystal packing and 7P7Y for the *Lk*ADH mutant Q126K. Quality indicators for the X-ray diffraction datasets and refinement results are given in Supplementary Table S1.

3. Results and Discussion

3.1. Transfer of Crystal Packing from LbADH to LkADH

Highly similar crystal packing of *Lb*ADH and *Lk*ADH is required to ensure that enhanced crystallizability of *Lk*ADH is caused by the transferred point mutation at the crystal contact. Since the *Lk*ADH variant described in the literature (PDB ID: 4RF4, [28]) does not form the same crystal contacts as *Lb*ADH, the sequence and crystallization conditions of *Lk*ADH were transferred from *Lb*ADH. For this purpose, His-tag and linker of *Lk*ADH were designed analogously to the *Lb*ADH wild type used before (PDB ID: 6H07; [27]).

Protein production and IMAC purification of His$_6$_GSG_*Lk*ADH (*Lk*ADH wild type) was implemented, resulting in purified and active *Lk*ADH wild type protein (SDS-PAGE and enzymatic activity are shown in Supplementary Figures S2 and S3). Crystallization of *Lk*ADH wild type in μL-scale applying conditions similar to *Lb*ADH (PEG MME 550, magnesium chloride, Tris/HCl, pH 7.0) yielded high quality protein crystals for X-ray diffraction (Supplementary Table S1). Analysis of X-ray diffraction data revealed a transformation of space group from *C121* (PDB ID: 4RF4; crystallization conditions: PEG 3350, magnesium formate, pH 7.0) to *I222*. Thus, by aligning amino acid tags and crystallization conditions, the crystal structure of *Lk*ADH could be transferred from a monoclinic crystal system (PDB ID: 4RF4) to an orthorhombic crystal system, as was observed with *Lb*ADH crystals. For the *Lb*ADH, it has been proven previously that a transition from space group *I222* to *P2$_1$22$_1$* does not alter the crystal contact areas significantly [27]. An alignment of *Lb*ADH and *Lk*ADH crystal structures of the tetramer reveals very high structural similarity (Figure 1) and highly similar crystal contacts (Supplementary Table S2), quantified by root-mean-square deviation (RMSD).
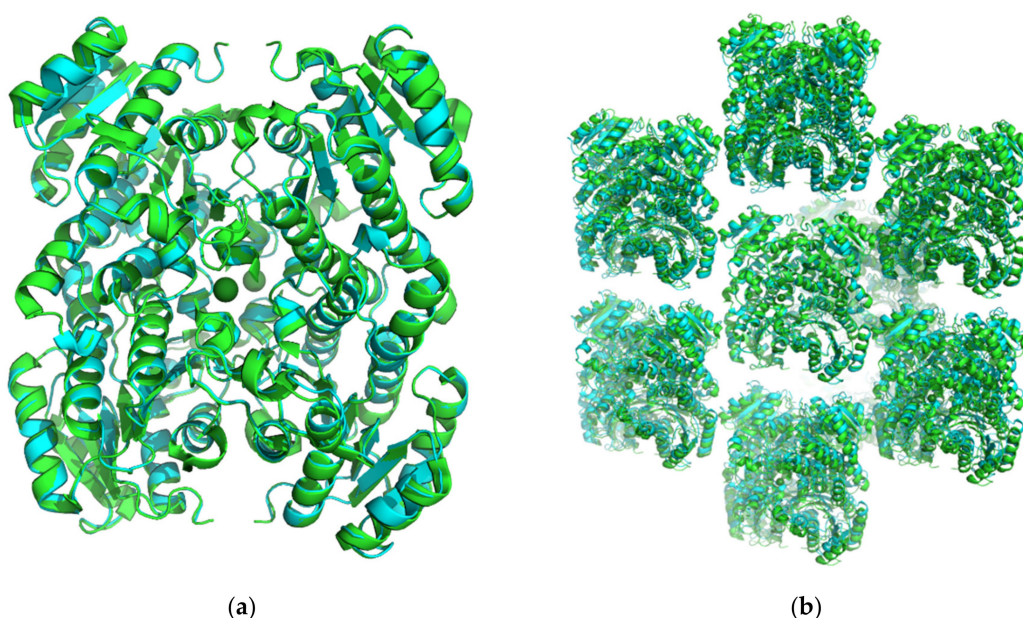

(**a**)   (**b**)

Figure 1. Structural alignment of *Lk*ADH (cyan; PDB ID: 7P36; R$_{work}$ = 0.9; R$_{free}$ = 0.11) and *Lb*ADH (green, PDB ID: 6H07) wild type (**a**) tetramers with RMSD$_{backbone}$ = 0.183 Å and RMSD$_{side chain}$ = 0.212 Å and (**b**) with selected symmetry related molecules in the crystal structure. Figures were generated with PyMOL (v.2.3; Schroedinger). The homotetramers are complexing two Mg^{2+} ions (dark green).

This study aims to prove the transfer of rational protein engineering at crystal contacts to a homologous protein. The requirement of similar crystal contact areas for the transfer could be met by adjusting the purification tag and crystallization conditions for *Lk*ADH analogously to *Lb*ADH resulting in the same crystal packing.

3.2. Transfer of Mutations on Crystal Contacts from LbADH to LkADH

In order to study the transfer of rational crystal contact engineering strategies established for *Lb*ADH, two out of four potential positions (K32, D54, T102, Q126) for the transfer of mutations on crystal contact areas of *Lb*ADH [24,25] were selected: T102 and Q126.

The choice of selecting T102 and Q126 was made by analyzing the crystal contacts of *Lk*ADH and comparing them to *Lb*ADH. In contrast to T102 and Q126, D54 is among the few amino acid positions that are noticeably different between *Lb*ADH and *Lk*ADH (expressed by a relatively high contact RMSD value of D54, see Supplementary Table S2). The symmetric crystal contact of D54 is packed more densely in *Lk*ADH than in *Lb*ADH,

indicating different interactions at this contact for *Lk*ADH. Position K32 in *Lb*ADH does not itself form a direct crystal contact, instead, mutant K32A contributes indirectly to the symmetric crystal contact at D54 by presumably reducing the screening of its electric field, as addressed in Nowotny et al. [25] and Hermann et al. [26]. Thus, the two crystal contact positions K32 and D54 were excluded as targets for the transfer of rational crystal contact engineering. The vicinity of the intermolecular crystal contact at position T102 and Q126 exhibits similar amino acid configurations for *Lb*ADH and *Lk*ADH wild type (Figure 2; contact RMSD in Supplementary Table S2). More importantly, the interaction targets of the introduced mutations, which are K48 for T102E and E44 for Q126K, reveal similar orientations in *Lb*ADH and *Lk*ADH wild type crystal structure alignment. Additionally, it was shown for *Lb*ADH that the selected mutants T102E and Q126K generated a salt bridge in *Lb*ADH crystals between negatively charged glutamic acid (E) and positive charged lysine (K) [26]. Thus, T102E and Q126K are the focus of this study.
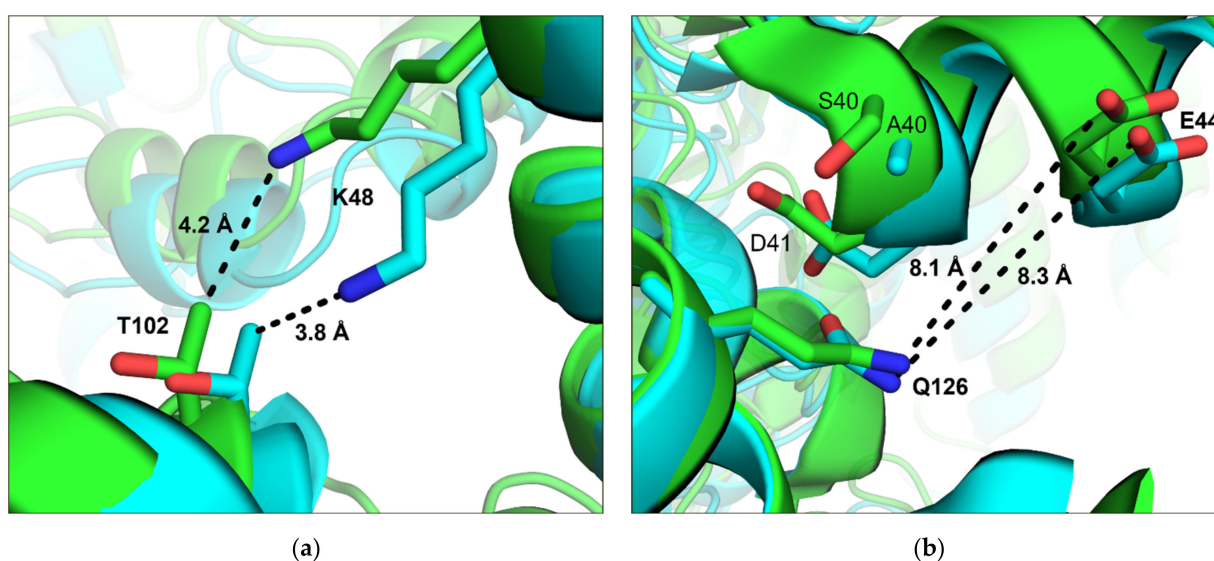

(a)   (b)

Figure 2. Illustration of *Lk*ADH (cyan) and *Lb*ADH (green) wild types' intermolecular crystal contacts at amino acid position (**a**) T102 and (**b**) Q126. Figures were generated and distances were calculated using PyMOL (v.2.3; Schroedinger).

Cloning of these two *Lk*ADH mutants was performed as described before. Protein production and downstream processing of mutant T102E and Q126K were accomplished, resulting in stable and pure protein solutions. *Lk*ADH protein solution purity after cell disruption, IMAC, dialysis and concentration as well as enzymatic activity of purified *Lk*ADH mutants is comparable to *Lk*ADH wild type (SDS-PAGE and enzymatic activity are shown in Supplementary Figures S2 and S3).

3.3. Stirred Crystallization of Dialyzed and Clarified E. coli Cell Lysate

Stirred batch crystallization studies with *E. coli* cell lysate were conducted with regard to the technical application of protein crystallization. First, stirred crystallization experiments were performed with clarified and additionally dialyzed *E. coli* cell lysate. During crystallization, the protein concentration of the supernatant decreases due to incorporation of *Lk*ADH molecules into the protein crystals. The protein concentration in the supernatant of mutant T102E decreases more rapidly than with *Lk*ADH wild type within the first 5 h (Figure 3). Furthermore, the protein concentration of T102E equilibrates at a lower level after 21 h of crystallization compared to *Lk*ADH wild type, a further characteristic for enhanced crystallizability and important for technical applications.
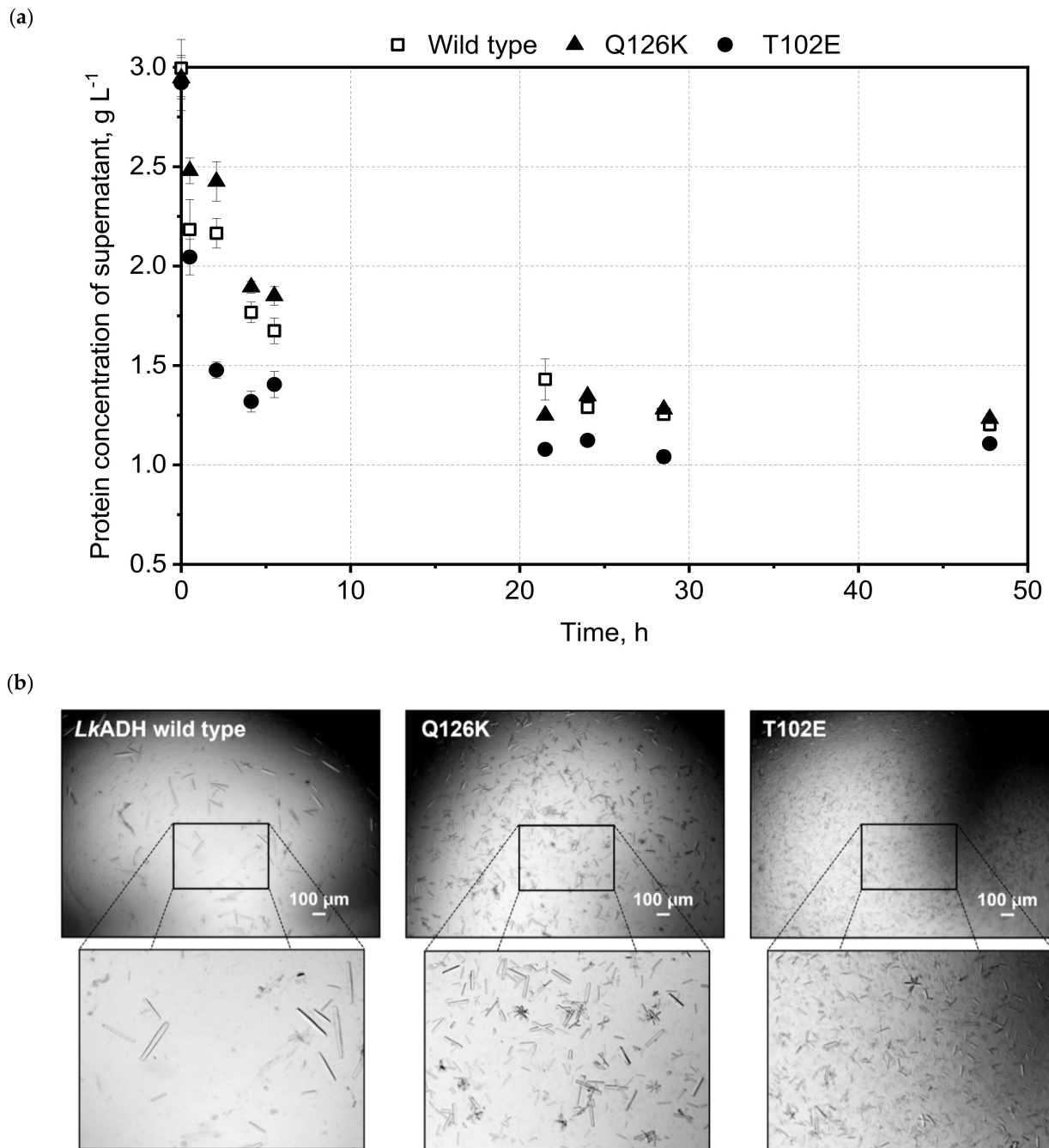
(a)

(b)

Figure 3. (**a**) Protein concentrations of clarified and dialyzed *E. coli* cell lysates of *Lk*ADH wild type and mutants T102E and Q126K. Batch crystallization was conducted in parallel stirred tank reactors (V = 5 mL, $n_{Stirrer}$ = 150 rpm, 20 °C, 100 g L^{-1} PEG MME 550). Protein concentration of supernatant was determined by BCA assay (n = 3); (**b**) Photomicrographs of *Lk*ADH wild type and mutants Q126K and T102E after 48 h of crystallization from clarified and dialyzed *E. coli* cell lysate in stirred tank reactors (c_0 = 3 g L^{-1}, V = 5 mL, $n_{Stirrer}$ = 150 rpm, 20 °C, 100 g L^{-1} PEG MME 550).

This reduced protein concentration at crystallization equilibrium and increased number of protein crystals of *Lk*ADH mutant T102E compared to the wild type *Lk*ADH has also been demonstrated previously for mutation T102E in *Lb*ADH ($P2_122_1$, PDB ID: 6Y0S) [24]. This indicates a successful transfer of a rational protein engineering strategy between homologous enzymes.

E. coli cell lysate still contains high amounts of host cell protein (HCP). Thus, crystallization yields quantified by total protein concentration measurements via BCA assay

are underestimated. This is due to remaining amounts of HCP in the solution and results in apparent crystallization yields of only 59–63% (Figure 4). Therefore, SDS-PAGE of the supernatants were performed before initiation of crystallization and at the end of the batch crystallization processes (48 h) and the results were compared densitometrically (Figure 4). The *Lk*ADH to HCP ratio in clarified and dialyzed cell lysate of *Lk*ADH mutants is similar to *Lk*ADH wild type. Comparing the SDS-PAGE bands of the *Lk*ADH variants before and after batch crystallization revealed a reduction in intensity of *Lk*ADH wild type protein concentration by 80%; whereas the intensity of *Lk*ADH mutants Q126K and T102E decreased by 85%, and about 95%, respectively (evaluated with GelAnalyzer, v.19.1). The crystallization yield of about 95% estimated by SDS-PAGE showed improved crystallization of mutant T102E, whereas no significant yield differences were identified between mutant Q126K and wild type *Lk*ADH.
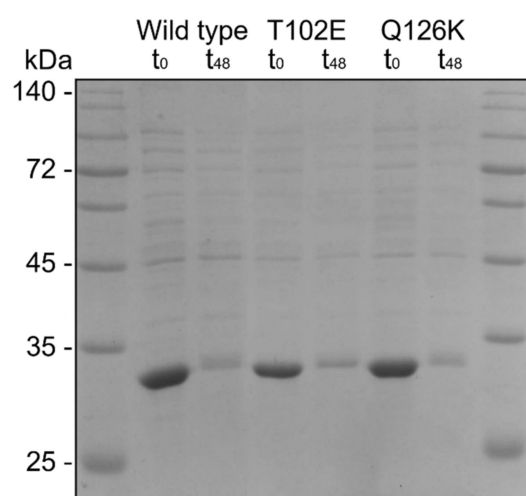

Figure 4. SDS-PAGE visualizing the protein content of clarified and dialyzed *E. coli* cell lysates of *Lk*ADH wild type and mutants T102E and Q126K. Depicted are samples of clarified and dialyzed *E. coli* cell lysates directly before crystallization initiation ($t_0 = 0$ h) and after 48 h (t_{48}) of crystallization in stirred tank reactors (V = 5 mL, $n_{Stirrer}$ = 150 rpm, 20 °C, 100 g L^{-1} PEG MME 550). *Lk*ADH variants are detected between 25–35 kDa, corresponding to its molecular monomer weight of 27.86 kDa (calculated with ExPASy ProtParam).

3.4. Evaluation of Crystal Size Differences between LkADH Variants

A higher number of crystals and a decrease in crystal size were observed with the protein mutants, compared to the wild type *Lk*ADH in the photomicrographs of the batch crystallization processes with clarified and dialyzed *E. coli* cell lysates (Figure 3b). For the quantification of crystal size differences in length and width between the *Lk*ADH variants, the photomicrographs were analyzed manually with imaging software (NIS Elements AR v.5.02, Nikon, Düsseldorf, Germany). The resulting protein crystal size distributions are shown in Figure 5. The frequency density of *Lk*ADH wild type crystals follows approximately a log-normal distribution with its mean length at 97.1 ± 29.5 µm (mean width: 11.4 ± 4.5 µm). A similar distribution is observed for the *Lk*ADH mutants, but with a shift of the mean crystal size to smaller crystal sizes by 40% for Q126K (mean length/width: 58.9 ± 9.8 µm/10.2 ± 2.9 µm) and by more than 70% for T102E (mean length/width: 27.5 ± 6.4 µm/5.9 ± 1.6 µm).

Comparing the crystals size to the wild type after stirred crystallization of *Lk*ADH mutants, the mean protein crystal size of *Lk*ADH mutants T102E and Q126K was reduced by more than 70% in length and 45% in width; and 40% in length and 10% in width, respectively (Figure 5), with a concomitant increase in the total amount of crystals (Figure 3b). This increase in the total number of crystals indicates a higher number of nucleation events for the mutants than occurred with the *Lk*ADH wild type. Stronger intermolecular interac-

tions compared to the wild type (see electron density map of the crystal contact of *Lk*ADH wild type and mutant Q126K with an additional salt-bridge in Supplementary Figure S4) can therefore be assumed to lead to an increased number of nucleation events. This correlation was already observed for *Lb*ADH mutants T102E and Q126K and supported on a molecular level by calculations of molecular dynamics free energy simulations [24,26].
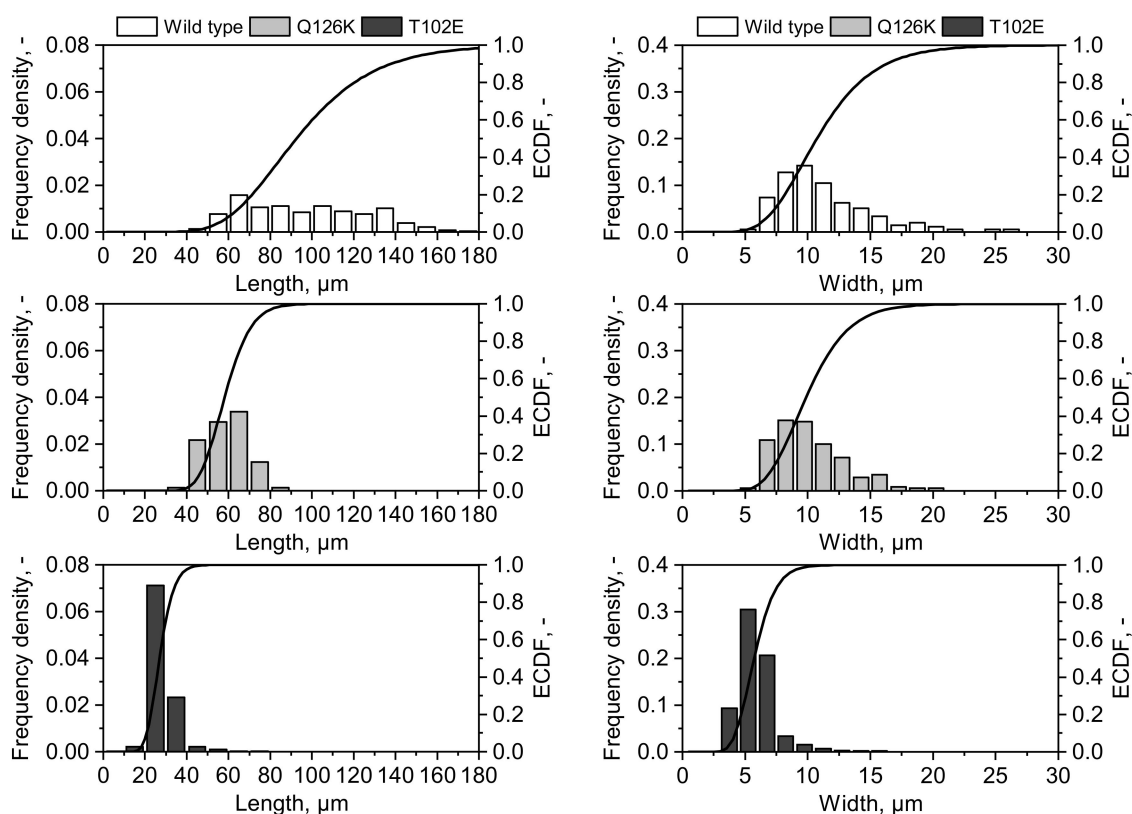

Figure 5. Protein crystal size distribution of *Lk*ADH wild type and mutants T102E and Q126K (Bar: Frequency density distribution; Line: Empirical cumulative distribution function). The distributions of length (**left**) and width (**right**) of the protein crystals formed after 48 h batch crystallization from clarified and dialyzed *E. coli* cell lysate in stirred tank reactors (c_0 = 3 g L^{-1}, V = 5 mL, $n_{Stirrer}$ = 150 rpm, 20 °C, 100 g L^{-1} PEG MME 550). The frequency density distribution of protein crystals in specific length/width classes in μm was evaluated with OriginPro 2020 (n = 335).

3.5. Stirred Crystallization of Clarified E. coli Cell Lysate

All batch protein crystallization processes were reproduced in the stirred tank reactors, without dialysis, after cell disruption and clarification (Figure 6). Due to the increased HCP concentrations without dialysis, no crystallization of *Lk*ADH wild type was observed within 48 h, but the mutants Q126K and T102E formed crystals as before.

Crystallization kinetics of the batch processes with clarified and dialyzed *E. coli* cell lysates, as shown before (Figure 3), as well as final crystallization yields estimated by SDS-PAGE (Figure 4), showed no significant differences in crystallizability between *Lk*ADH wild type and the mutant Q126K. Clear differences were identified in the final protein crystal size distributions of both proteins, showing an increase in nucleation events with *Lk*ADH mutants compared to *Lk*ADH wild type under the conditions studied (Figure 5). A small variation of these conditions caused by batch crystallizations of clarified *E. coli* lysates without dialysis resulted in no nucleation events within 48 h with the *Lk*ADH wild type (Figure 6). As the crystallizability of proteins is not well-defined, it may be concluded that comparing final protein crystal size distribution and the number of crystals may be a practical measure for defining an order of crystallizability: An increased final crystal number with reduced crystal sizes means better crystallizability compared to other

proteins under the same crystallization conditions. Applying this measure to the *Lk*ADH proteins studied results in an order of crystallizability: T102E > Q126K > *Lk*ADH wild type. A comparison of this ranking with *Lb*ADH [24,26] reveals the identical order of crystallizability, further validating the rational approach of the protein engineering strategy transfer between homologous enzymes.
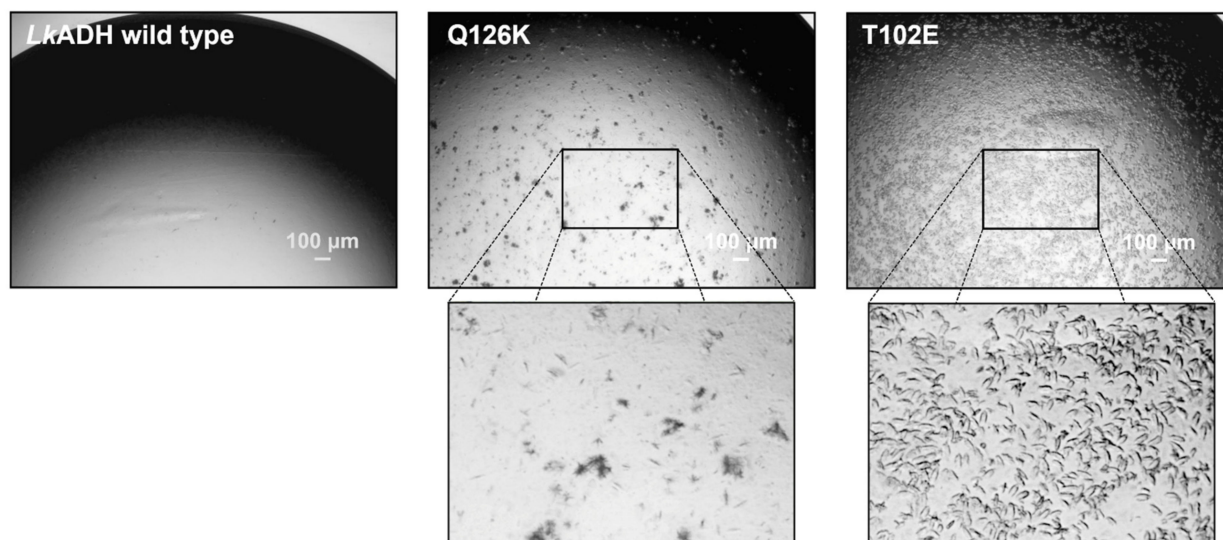

Figure 6. Photomicrographs of *Lk*ADH wild type and mutants Q126K and T102E after 48 h of crystallization from clarified *E. coli* cell lysate without dialysis in stirred tank reactors ($c_0 = 5$ g L^{-1}, V = 5 mL, $n_{Stirrer} = 150$ rpm, 20 °C, 150 g L^{-1} PEG MME 550).

3.6. Comparison of LkADH and LbADH Crystal Contacts at Position Q126 on a Molecular Level

For further evidence of effective transfer of crystal contact mutations, the introduced single amino acid mutations in *Lk*ADH will be considered at molecular level and compared to the respective *Lb*ADH mutants. Since the protein crystallization of *Lk*ADH mutant T102E occurs so rapidly, the crystals obtained were too small for X-ray analysis using non-microfocus X-ray beamline. Therefore, the X-ray crystal structure of *Lk*ADH mutant Q126K is discussed below.

Comparing the position 126 in *Lk*ADH wild type (Figure 2) and mutant Q126K (Figure 7a), the interacting amino acid has changed. In contrast to Q126 interacting weakly with D41, Q126K developed a strong interaction with E44, resulting in a salt bridge between the ammonium group of the lysine side chain (K) and the carboxylate group of glutamic acid (E). This establishment of interaction with E44 is also observed for *Lb*ADH mutant Q126K (Figure 7b).

Comparison of the crystal contact at position Q126K reveals the same interaction partner for both *Lb*ADH and *Lk*ADH. The interacting amino acids K126 and E44 in *Lk*ADH are more closely located (2.8 Å distance), indicating a stronger interaction than in *Lb*ADH Q126K (3.9 Å distance, evaluated with PyMOL, v.2.3.; Schroedinger). Additionally, the *Lb*ADH Q126K crystal structure presents two possible conformations for both amino acids E44 and K126, suggesting a more flexible interaction at this position. One of the possible conformations of E44 is even facing away from K126. Recent molecular dynamic studies determined the formation of the salt bridge between K126 and E44 in about 65% of the simulated time frames for *Lb*ADH [26]. Contrary to *Lb*ADH, the crystal structure of *Lk*ADH mutant Q126K reveals one conformation for the K126-E44 crystal contact with E44 pointing directly to K126, which is well-defined in the electron density map (Supplementary Figure S4b). This single conformation indicates a stronger intermolecular interaction, suggesting an enhanced crystallizability for the transfer of mutant Q126K from *Lb*ADH to *Lk*ADH. To confirm this assumption, further calculations of molecular dynamics free energy simulations of this crystal contact are necessary. To conclude, the transfer of interacting

amino acids in mutant Q126K was successfully transferred from *Lb*ADH to *Lk*ADH, with a tendency towards a stronger crystal contact formation in *Lk*ADH.
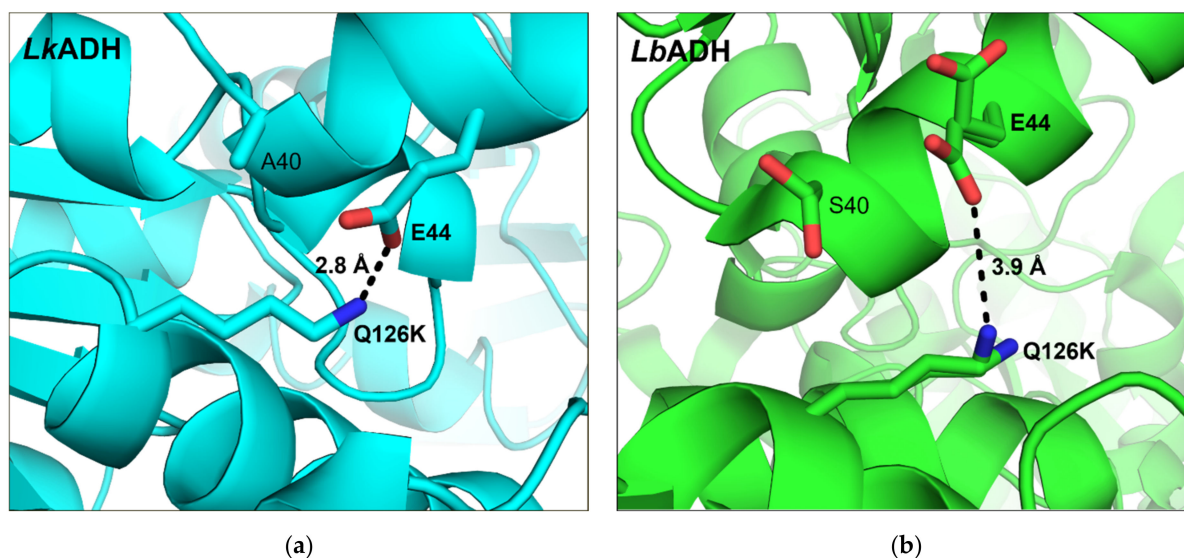

(**a**)　　　　　　　　　　　　　　　　　　　　　　　　　　　(**b**)

Figure 7. Illustration of crystal contact Q126K in (**a**) *Lk*ADH (PDB ID: 7P7Y) and (**b**) *Lb*ADH (PDB ID: 6Y0Z) with interaction partner E44. Distances were calculated using PyMOL (v.2.3; Schroedinger).

Based on the evaluation of stirred crystallization experiments and considerations at the molecular level, *Lk*ADH mutants T102E and Q126K are more favorable for technical applications than *Lk*ADH wild type in terms of crystallizability. This is because the main objective for technical protein crystallization is to achieve rapid and efficient protein crystallization [39] to increase the space-time yield of the process. Considering the technical application of protein crystallization from impure sources as a purification step, future work should investigate the purity of the crystals.

This study shows that the results of rational crystal contact engineering of *Lb*ADH can be transferred successfully to the homologous *Lk*ADH. To advance the establishment of a more general approach to enhance protein crystallization by rational crystal contact engineering, developed strategies for *Lb*ADH and *Lk*ADH will be extended further to non-homologous proteins.

Supplementary Materials: The following are available online at https://www.mdpi.com/article/10.3390/cryst11080975/s1, Figure S1: Sequence alignment of *Lk*ADH and *Lb*ADH wild type with an amino acid sequence homology of 88.5 %. The optimal global alignment was generated with the Needleman-Wunsch algorithm (EMBOSS, output format: pair, matrix: BLOSUM62) [1]. Identical amino acids are marked with an asterisk. Crystal contacts (distance between amino acids < 4 Å) are marked for *Lk*ADH (cyan) and *Lb*ADH (green). The positions selected for mutations, T102 and Q126, are underlined. RMSD of the crystal contacts are listed in Supplementary Table S2. Figure S2: Illustration of protein purity analysis using SDS-PAGE of *Lk*ADH wild type (WT) and mutants Q126K (K) and T102E (E). The proteins purified by IMAC were loaded onto a 12.5% SDS gel (2.5 μg protein) under reducing conditions. Bands between 25–35 kDa correspond to *Lk*ADH monomers. Figure S3: Maximum relative enzymatic activity of *Lk*ADH mutants Q126K and T102E compared to *Lk*ADH wild type. Purified protein solutions of *Lk*ADH variants were adjusted to 6 mg L^{-1}. Enzymatic activity was measured for 10 min at 340 nm (45 °C) with addition of 180 μL buffer (20 mM HEPES, pH 7.0; 1 mM MgCl$_2$) containing 0.5 mM NADPH and 10 mM acetophenone to a final volume of 200 μL (n = 3). Figure S4: Electron density map (blue) of *Lk*ADH crystal contact at position (a) Q126 and (b) Q126K with well-defined electron density of the lysine and glutamic acid side chain. The map represents the structure factor amplitude difference 2F$_o$ – F$_c$ with a contour level of 1.0 σ (calculated with *REFMAC* [2]). Table S1: Data collection and refinement statistics of X-ray diffraction experiments of *Lk*ADH wild type and mutant Q126K crystals (values in parentheses are for highest resolution

shell). Table S2: RMSD$_{\text{side chain}}$ of crystal contacts present in both *Lk*ADH and *Lb*ADH wild type and calculated after side chain and backbone alignment of one tetramer. Crystal contacts were defined by a distance < 4 Å between amino acid residues of neighboring tetramers. The contact RMSD$_{\text{side chain}}$ was then calculated by alignment of those amino acid residues forming a contact with PyMOL (v.2.3.; Schroedinger). Therefore, a smaller contact RMSD value indicates, that the corresponding crystal contacts in *Lb*ADH and *Lk*ADH wild type crystals are locally more similar.

Author Contributions: Conceptualization, B.W. and D.B.; methodology, B.W. and N.v.d.E.; validation, B.W. and D.B.; investigation, B.W.; X-ray resources and diffraction experiments, R.J. and D.N.; writing—original draft preparation, B.W.; writing—review and editing, B.W., D.B., D.W.-B., and R.J.; supervision, D.W.-B. All authors have read and agreed to the published version of the manuscript.

Data Availability Statement: All X-ray crystal structure data in this study have been deposited and are available in the Protein Data Bank under the identification codes 7P36 and 7P7Y. All other data generated or analyzed during this study are included in this article and the Supplementary Material or are available from the corresponding author upon reasonable request.

Conflicts of Interest: The authors declare no conflict of interest.

References

1. Newman, J.; Fazio, V.J.; Lawson, B.; Peat, T.S. The C6 Web Tool: A Resource for the Rational Selection of Crystallization Conditions. *Cryst. Growth Des.* **2010**, *10*, 2785–2792. [CrossRef]
2. Weber, P.; Pissis, C.; Navaza, R.; Mechaly, A.E.; Saul, F.; Alzari, P.M.; Haouz, A. High-Throughput Crystallization Pipeline at the Crystallography Core Facility of the Institut Pasteur. *Molecules* **2019**, *24*, 4451. [CrossRef]
3. Longenecker, K.L.; Garrard, S.M.; Sheffield, P.J.; Derewenda, Z.S. Protein crystallization by rational mutagenesis of surface residues: Lys to Ala mutations promote crystallization of RhoGDI. *Acta Crystallogr. Sect. D Biol. Crystallogr.* **2001**, *57*, 679–688. [CrossRef]
4. Lawson, D.M.; Artymiuk, P.J.; Yewdall, S.J.; Smith, J.M.; Livingstone, J.C.; Treffry, A.; Luzzago, A.; Levi, S.; Arosio, P.; Cesareni, G.; et al. Solving the structure of human H ferritin by genetically engineering intermolecular crystal contacts. *Nature* **1991**, *349*, 541–544. [CrossRef]
5. Braig, K.; Otwinowski, Z.; Hegde, R.; Boisvert, D.C.; Joachimiak, A.; Horwich, A.L.; Sigler, P.B. The crystal structure of the bacterial chaperonln GroEL at 2.8 Å. *Nature* **1994**, *371*, 578–586. [CrossRef]
6. Horwich, A. Working with Paul Sigler. *Nat. Struct. Biol.* **2000**, *7*, 269–270. [CrossRef] [PubMed]
7. McElroy, H.E.; Sisson, G.W.; Schoettlin, W.E.; Aust, R.M.; Villafranca, J.E. Studies on engineering crystallizability by mutation of surface residues of human thymidylate synthase. *J. Cryst. Growth* **1992**, *122*, 265–272. [CrossRef]
8. Derewenda, Z.S. The use of recombinant methods and molecular engineering in protein crystallization. *Methods* **2004**, *34*, 354–363. [CrossRef] [PubMed]
9. Derewenda, Z.S.; Vekilov, P.G. Entropy and surface engineering in protein crystallization. *Acta Crystallogr. Sect. D Biol. Crystallogr.* **2006**, *62*, 116–124. [CrossRef] [PubMed]
10. Cooper, D.R.; Boczek, T.; Grelewska, K.; Pinkowska, M.; Sikorska, M.; Zawadzki, M.; Derewenda, Z. Protein crystallization by surface entropy reduction: Optimization of the SER strategy. *Acta Crystallogr. Sect. D Biol. Crystallogr.* **2007**, *63*, 636–645. [CrossRef]
11. Derewenda, Z.S.; Godzik, A. The "Sticky Patch" Model of Crystallization and Modification of Proteins for Enhanced Crystallizability. *Methods Mol. Biol.* **2017**, *1607*, 77–115. [CrossRef]
12. Derewenda, Z.S. Protein crystallization in drug design: Towards a rational approach. *Expert Opin. Drug Discov.* **2007**, *2*, 1329–1340. [CrossRef] [PubMed]
13. Derewenda, Z.S. Rational protein crystallization by mutational surface engineering. *Structure* **2004**, *12*, 529–535. [CrossRef]
14. Laganowsky, A.; Zhao, M.; Soriaga, A.B.; Sawaya, M.R.; Cascio, D.; Yeates, T.O. An approach to crystallizing proteins by metal-mediated synthetic symmetrization. *Protein Sci* **2011**, *20*, 1876–1890. [CrossRef]
15. Devedjiev, Y.; Surendranath, Y.; Derewenda, U.; Gabrys, A.; Cooper, D.R.; Zhang, R.-g.; Lezondra, L.; Joachimiak, A.; Derewenda, Z.S. The Structure and Ligand Binding Properties of the B.subtilis YkoF Gene Product, a Member of a Novel Family of Thiamin/HMP-binding Proteins. *J. Mol. Biol.* **2004**, *343*, 395–406. [CrossRef]
16. Roosen-Runge, F.; Zhang, F.; Schreiber, F.; Roth, R. Ion-activated attractive patches as a mechanism for controlled protein interactions. *Sci. Rep.* **2014**, *4*, 7016. [CrossRef]

17.   Banatao, D.R.; Cascio, D.; Crowley, C.S.; Fleissner, M.R.; Tienson, H.L.; Yeates, T.O. An approach to crystallizing proteins by synthetic symmetrization. *Proc. Natl. Acad. Sci. USA* **2006**, *103*, 16230–16235. [CrossRef]

18.   Hekmat, D. Large-scale crystallization of proteins for purification and formulation. *Bioprocess Biosyst. Eng.* **2015**, *38*, 1209–1231. [CrossRef] [PubMed]

19.   Dos Santos, R.; Carvalho, A.L.; Roque, A.C.A. Renaissance of protein crystallization and precipitation in biopharmaceuticals purification. *Biotechnol. Adv.* **2017**, *35*, 41–50. [CrossRef]

20.   Shenoy, B.; Wang, Y.; Shan, W.; Margolin, A.L. Stability of crystalline proteins. *Biotechnol. Bioeng.* **2001**, *73*, 358–369. [CrossRef] [PubMed]

21.   Brange, J.; Vølund, A. Insulin analogs with improved pharmacokinetic profiles. *Adv. Drug Deliv. Rev.* **1999**, *35*, 307–335. [CrossRef]

22.   Liu, Y.; Hou, H.; Li, J.; Cheng, Q.-D.; Zhang, X.; Zeng, X.-B.; Fiaz, A.; Wang, B.; Zhang, C.-Y.; Lu, Q.-Q.; et al. Direct Crystallization of Proteins from Impure Sources. *Cryst. Growth Des.* **2020**, *20*, 1694–1705. [CrossRef]

23.   Harrison, R.G.; Todd, P.W.; Rudge, S.R.; Petrides, D.P. *Bioseparations Science and Engineering*, 2nd ed.; Oxford University Press: New York, NY, USA, 2003.

24.   Grob, P.; Huber, M.; Walla, B.; Hermann, J.; Janowski, R.; Niessing, D.; Hekmat, D.; Weuster-Botz, D. Crystal Contact Engineering Enables Efficient Capture and Purification of an Oxidoreductase by Technical Crystallization. *Biotechnol. J.* **2020**, e2000010. [CrossRef] [PubMed]

25.   Nowotny, P.; Hermann, J.; Li, J.; Krautenbacher, A.; Klöpfer, K.; Hekmat, D.; Weuster-Botz, D. Rational Crystal Contact Engineering of Lactobacillus brevis Alcohol Dehydrogenase To Promote Technical Protein Crystallization. *Cryst. Growth Des.* **2019**, *19*, 2380–2387. [CrossRef]

26.   Hermann, J.; Bischoff, D.; Grob, P.; Janowski, R.; Hekmat, D.; Niessing, D.; Zacharias, M.; Weuster-Botz, D. Controlling Protein Crystallization by Free Energy Guided Design of Interactions at Crystal Contacts. *Crystals* **2021**, *11*, 588. [CrossRef]

27.   Hermann, J.; Nowotny, P.; Schrader, T.E.; Biggel, P.; Hekmat, D.; Weuster-Botz, D. Neutron and X-ray crystal structures of Lactobacillus brevis alcohol dehydrogenase reveal new insights into hydrogen-bonding pathways. *Acta Crystallogr. Sect. F* **2018**, *74*, 754–764. [CrossRef]

28.   Noey, E.L.; Tibrewal, N.; Jiménez-Osés, G.; Osuna, S.; Park, J.; Bond, C.M.; Cascio, D.; Liang, J.; Zhang, X.; Huisman, G.W.; et al. Origins of stereoselectivity in evolved ketoreductases. *Proc. Natl. Acad. Sci. USA* **2015**, *112*, E7065–E7072. [CrossRef]

29.   Zheng, L.; Baumann, U.; Reymond, J.L. An efficient one-step site-directed and site-saturation mutagenesis protocol. *Nucleic Acids Res.* **2004**, *32*, e115. [CrossRef]

30.   Gasteiger, E.H.C.; Gattiker, A.; Duvaud, S.; Wilkins, M.R.; Appel, R.D.; Bairoch, A. Protein Identification and Analysis Tools on the ExPASy Server. In *The Proteomics Protocols Handbook*; Walker, J.M., Ed.; Humana Press: Totowa, NJ, USA, 2005; pp. 571–607.

31.   Smejkal, B.; Agrawal, N.J.; Helk, B.; Schulz, H.; Giffard, M.; Mechelke, M.; Ortner, F.; Heckmeier, P.; Trout, B.L.; Hekmat, D. Fast and scalable purification of a therapeutic full-length antibody based on process crystallization. *Biotechnol. Bioeng.* **2013**, *110*, 2452–2461. [CrossRef]

32.   Hebel, D.; Ürdingen, M.; Hekmat, D.; Weuster-Botz, D. Development and Scale up of High-Yield Crystallization Processes of Lysozyme and Lipase Using Additives. *Cryst. Growth Des.* **2013**, *13*, 2499–2506. [CrossRef]

33.   Teng, C.C.; Man, H.T. Simple reflection technique for measuring the electro-optic coefficient of poled polymers. *Appl. Phys. Lett.* **1990**, *56*, 1734–1736. [CrossRef]

34.   Kabsch, W. XDS. *Acta Crystallogr. Sect. D* **2010**, *66*, 125–132. [CrossRef] [PubMed]

35.   Winn, M.D.; Ballard, C.C.; Cowtan, K.D.; Dodson, E.J.; Emsley, P.; Evans, P.R.; Keegan, R.M.; Krissinel, E.B.; Leslie, A.G.; McCoy, A.; et al. Overview of the CCP4 suite and current developments. *Acta Crystallogr. Sect. D Biol. Crystallogr.* **2011**, *67*, 235–242. [CrossRef] [PubMed]

36.   McCoy, A.J.; Grosse-Kunstleve, R.W.; Adams, P.D.; Winn, M.D.; Storoni, L.C.; Read, R.J. Phaser crystallographic software. *J. Appl. Crystallogr.* **2007**, *40*, 658–674. [CrossRef] [PubMed]

37.   Emsley, P.; Lohkamp, B.; Scott, W.G.; Cowtan, K. Features and development of Coot. *Acta Crystallogr. Sect. D* **2010**, *66*, 486–501. [CrossRef]

38.   Murshudov, G.N.; Vagin, A.A.; Dodson, E.J. Refinement of Macromolecular Structures by the Maximum-Likelihood Method. *Acta Crystallogr. Sect. D* **1997**, *53*, 240–255. [CrossRef]

39.   Schmidt, S.; Havekost, D.; Kaiser, K.; Kauling, J.; Henzler, H.-J. Crystallization for the Downstream Processing of Proteins. *Eng. Life Sci.* **2005**, *5*, 273–276. [CrossRef]